

NON-PARAMETRIC RECONSTRUCTION OF ABELL 2218* FROM COMBINED WEAK AND STRONG LENSING

HANADI M. ABDELSALAM, PRASENJIT SAHA

Department of Physics (Astrophysics), Keble Rd., OX1 3RH, Oxford, UK.

AND

LILIYA L.R. WILLIAMS

Institute of Astronomy, Madingley Rd., CB3 0HA, Cambridge, UK.

Accepted version July 16, 1998

ABSTRACT

We apply a new non-parametric technique to reconstruct, with uncertainties, the projected mass distribution of the inner region of Abell 2218, using combined strong and weak lensing constraints from multiple-image systems and arclets with known redshifts. The reconstructed mass map broadly resembles previous, less detailed, parametric models, but when examined in detail shows several sub-structures, not necessarily associated with light but strongly required by the lensing data. In particular, the highest mass peak is offset by $\sim 30h_{50}^{-1}$ kpc from the main light peak, and projected mass-to-light in the directions of different cluster galaxies varies by at least a factor of 10. On comparing with mass estimates from models of the X-ray emitting gas, we find that the X-ray models under-predict the enclosed mass profile by, *at least* a factor of 2.5; the discrepancy gets worse if we assume that mass traces light to the extent allowed by the lensing constraints.

Subject headings: Dark matter - galaxies: clusters: individual (Abell 2218) - gravitational lensing: weak & strong lensing - X-ray

1. INTRODUCTION

Galaxy clusters are thought to be the largest and most recently assembled gravitationally bound entities in the universe and, thus, an accurate determination of their masses is of utmost importance to full understanding of the formation and evolution of cosmic structures, mapping of dark matter in large scales and for constraining cosmological parameters. Traditional methods for inferring mass distributions in clusters are (i) dynamical methods, in which the observed line-of-sight velocity distribution of the luminous cluster galaxies is used in conjunction with the virial theorem, and (ii) X-ray methods, in which the investigation of the X-ray emission of the intra-cluster hot gas is used to trace the cluster potential. Both these traditional methods depend on restrictive assumptions about the geometrical and dynamical state of clusters. A more sophisticated method, which proved to be very reliable and independent of any prior assumptions, is gravitational lensing.

Theoretically, the above three methods have to

yield the same cluster masses if the clusters are dynamically relaxed, but recent literature shows a lot of discussion of and disagreement of cluster masses derived from observed velocity dispersions, observations of X-ray emitting gas and gravitational lensing (Miralda-Escudé and Babul 1995, Wu and Fang 1997). Early studies based upon few selected clusters claimed a mass estimate discrepancy of at least $\sim 2 - 3$ among them. This discrepancy can well be attributed to projection effects, non-thermal pressure or the specific cluster is still in the formation era. Evidently, the problem is relevant to the precise determination of mass distribution and to the dynamical evolution of those clusters. For clusters which are still in an ongoing merging phase, i.e., not in hydrostatic equilibrium, the hot gas does not follow the gravitational potential of the cluster and thereby the X-ray cluster mass is uncertain and should be different from the gravitational lensing-derived mass and/or even the virial mass.

Within gravitational lensing, there are two distinct

*Based on observations made with the NASA/ESA Hubble Space Telescope, obtained from the data archive at the Space Telescope Science Institute. STScI is operated by the association of universities for research in Astronomy, Inc. under the NASA contract N-AS 5-26555.

methods for inferring masses from lensing observations; (i) the parametric model-fitting method for the strong lensing region (giant arcs and multiple images), and (ii) statistical distortion method for the weak lensing regions (weakly distorted single arclets). The parametric model-fitting starts from the inner most regions of galaxy cluster, where lensing information is richest and extends outwards. It requires fitting parametrized profiles to cluster-sized galaxies (Kneib et al. 96 [hereafter KESCS96]). It works efficiently with one or two multiple image systems but becomes difficult to implement with several multiple image systems spanning outwards and hence the fitted model becomes non-unique. On the other hand, the statistical distortions method starts from regions where the distortions are very tiny and weak, i.e outer regions of galaxy clusters, and goes inwards. It requires averaging statistically the ellipticities of background galaxies over patches of sky, typically $\sim 20''$ in size, to trace the cluster mass distribution from its shear field (Kaiser and Squires 1993 [hereafter KS93], Kaiser 1995, Schneider and Seitz 1995). Methods, which are based on KS93 algorithm, suffer from a global invariance transformation known as the ‘‘mass-sheet-degeneracy’’ and also cannot be used to probe the inner regions of rich clusters, because the lensing properties change very rapidly over that sampling scale.

In intermediate regions, with no occurrence of multiple images but having highly distorted arclets, neither of the above methods can be used. However, several attempts to reconstruct the mass distribution in this region were made (Kaiser 95, Schneider and Seitz 1995, Seitz & Schneider 1996), but their formulation of the problem made it non-linear and still suffer from the so called mass-sheet degeneracy and boundary effects.

Obviously, the problem of mapping the cluster mass distribution from gravitational lensing require an independent non-parametric method that can be used simultaneously in regions with varying lensing strength. The required method should disentangle the systematic effects that plagued the existing methods encoded in forms of non-uniqueness.

In this paper we present a new and general reconstruction technique that combines regions with varying lensing strength the strong and overcomes the drawbacks of the existing methods. The technique is basically an extension of the non-parametric cluster inversion described by AbdelSalam et al. (1998) [hereafter Paper I] for the strong lensing regime to incorporate the extra information encoded in the observations of single/weakly distorted arclets. The extension results in a method that combines strong and weak lensing data in a mass reconstruction and over-

comes the mass sheet degeneracy. In general, the method is non-parametric and similar to the weak lensing (or statistical distortions) method of KS93, but our formulation of the problem is manifestly linear in all the regimes and hence the problem becomes simpler and can thereby easily include the strong lensing regime.

We apply the technique to the spectacular cluster-lens A2218 to reconstruct its projected mass distribution, with uncertainties, from combined strong and weak lensing. This cluster has previously been studied through parametric lens modeling of strong lensing and arcs by Kneib et al. (1995) and KESCS96, non-parametric inversion from statistical distortions by Squires et al. (1996), and parametric modeling of statistical distortions by Smail et al. (1997).

2. THE RECONSTRUCTION METHOD

The method we will follow here is a free-form or non-parametric one that reconstructs a pixellated mass distribution. It is basically the same as in Paper I, except that (a) in this work we implement constraints from weak as well as strong lensing whereas the earlier work implemented only strong lensing and described the extension to weak lensing, and (b) this paper uses Gaussian pixels whereas Paper I used square pixels—the difference is tiny for the results of either paper. Since Paper I already has a full description, we will only summarize the technique here.

2.1. Pixellization of the mass distribution

The lens plane is divided into $N \times N$ pixels with inter-pixel distance a . The mn th pixel is a Gaussian tent with ‘dispersion’ $a/2$ and peak height κ_{mn} . That is to say, if the mn -th pixel is centered at $\boldsymbol{\theta}_{mn}$ it has a mass profile

$$\kappa_{mn} \exp\left(\frac{-2(\boldsymbol{\theta} - \boldsymbol{\theta}_{mn})^2}{a^2}\right). \quad (2-1)$$

Hereafter, we refer to a as the pixel size. We measure κ_{mn} in units of the critical density Σ_{crit} for sources at infinity. Thus the total mass is

$$M_{\text{total}} = \frac{a^2 \pi}{2} \Sigma_{\text{crit}} \sum_{mn} \kappa_{mn}. \quad (2-2)$$

The appropriately scaled arrival time of a light ray from a background source at an unlensed angular position $\boldsymbol{\beta}$ via a point $\boldsymbol{\theta}$ in the pixellated lens plane to the observer is

$$\tau(\boldsymbol{\theta}) = \frac{1}{2}(\boldsymbol{\theta} - \boldsymbol{\beta})^2 - \frac{D_{ds}}{D_s} \sum_{mn} \kappa_{mn} \psi_{mn}(\boldsymbol{\theta}), \quad (2-3)$$

where

$$\psi_{mn}(\boldsymbol{\theta}) = \frac{1}{\pi} \int \exp\left(\frac{-2(\boldsymbol{\theta}' - \boldsymbol{\theta}_{mn})^2}{a^2}\right) \ln|\boldsymbol{\theta} - \boldsymbol{\theta}'| d^2\boldsymbol{\theta}'. \quad (2-4)$$

Thus, $\kappa_{mn}\psi_{mn}(\boldsymbol{\theta})$ represents the contribution of the mn -th pixel to the total gravitational potential of the lens. Its derivatives with respect to $\boldsymbol{\theta}$ represent contributions to the bending angle and amplification components.

See Appendix A for explicit expressions for the function ψ_{mn} and its derivatives.

2.2. Lensing observables and constraint equations

The basic approach of our technique is that the lens equation ($\nabla\tau(\boldsymbol{\theta}) = 0$) and shape parameters or distortions of gravitationally lensed images ($\nabla\nabla\tau(\boldsymbol{\theta})$), all at $\boldsymbol{\theta}$ values corresponding to the observed image locations, are considered as rigid linear constraints on the mass distribution.

Writing the lens equation at an observed image location $\boldsymbol{\theta}_1$

$$\boldsymbol{\beta} = \boldsymbol{\theta}_1 - \frac{D_{ds}}{D_s} \sum_{mn} \kappa_{mn} \nabla\boldsymbol{\theta} \psi_{mn}(\boldsymbol{\theta}_1), \quad (2-5)$$

each image supplies us with two-component constraint equation. But we have to solve for the unknown source position $\boldsymbol{\beta}$. Thus the number of constraints on the mass distribution from multiple images is $2(\langle\text{images}\rangle - \langle\text{sources}\rangle)$. These strong lensing constraints are linear equality constraints.

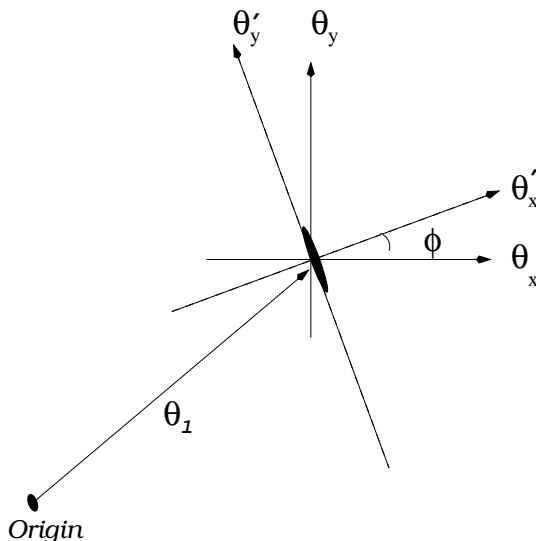


Figure 1. Illustration of the notation used in the text for explaining the constraints from weak lensing. The $\theta_{x'}, \theta_{y'}$ axes are the principal axes of the observed stretched arclet, and are rotated by an observed angle ϕ with respect to the main coordinate axes θ_x, θ_y .

The constraints from the observed shape parameters of distorted images (arclets) can be obtained from the the Hessian of the arrival time function. If an arclet at $\boldsymbol{\theta}_1$ is observed to be stretched along the direction $\boldsymbol{\theta}_{y'}$ by at least a factor of ϵ compared to the perpendicular direction $\boldsymbol{\theta}_{x'}$ (see Fig. 1), then by considering the $\theta_{x'}, \theta_{y'}$ components of the inverse amplification matrix we have

$$\epsilon \left| \frac{\partial^2}{\partial\theta_{x'}^2} \tau(\boldsymbol{\theta}_1) \right| \leq \left| \frac{\partial^2}{\partial\theta_{y'}^2} \tau(\boldsymbol{\theta}_1) \right|. \quad (2-6)$$

If we can independently infer the image parity we can remove the absolute value signs in equation (2-6), which will then supply us with a linear constraint equation on the κ_{mn} , because rotation to $\theta_{x'}, \theta_{y'}$ coordinates is a linear transformation.

While constraints of the form (2-6) can be used for arclets in multiply-imaged systems (and we do so), they are most useful for singly imaged arclets (weak lensing). For statistical distortions the form of the constraint stays exactly the same. If the shear field is known accurately enough the inequality can become an equality, and can be supplemented by the additional constraint

$$\frac{\partial^2}{\partial\theta_{x'}\partial\theta_{y'}} \tau(\boldsymbol{\theta}_1) = 0. \quad (2-7)$$

In our work the weak lensing constraints are expressed in implicit form (Eq. 2-6), whereas in previous work (e.g. KS93, Kaiser 1995, Seitz & Schneider 1996) it is usual to express these in explicit form. The advantage of the implicit form is that the constraints remain linear in all lensing regimes.

2.3. Breaking the mass sheet degeneracy

The mass sheet degeneracy is as follows. Consider the lens equation in the form

$$\boldsymbol{\beta} = \boldsymbol{\theta} - \frac{D_{ds}}{D_s} \boldsymbol{\alpha}. \quad (2-8)$$

The transformation

$$\boldsymbol{\alpha} \rightarrow r\boldsymbol{\alpha} + \frac{D_s}{D_{ds}}(1-r)\boldsymbol{\theta}, \quad \boldsymbol{\beta} \rightarrow r\boldsymbol{\beta} \quad (2-9)$$

simply amounts to multiplying both sides of Eq. (2-8) by r . Clearly, image positions will be unaffected by such a transformation. Also, since the magnification matrix is just $\partial\boldsymbol{\theta}/\partial\boldsymbol{\beta}$ the transformation will just rescale the whole matrix by r^{-1} ; in other words, relative shear and magnifications will be unaffected but absolute amplification will change. Physically, the transformation (2-9) amounts to rescaling the mass

everywhere and then adding a constant mass sheet; hence the name mass-sheet degeneracy.

It is sometimes thought that measuring absolute amplifications is the only way to break the mass-sheet degeneracy. This is not so. It is easy to verify that the transformation (2-9) will not have the same invariance property for two different source redshifts at the same time. Thus lensing data with more than one source redshift breaks the mass-sheet degeneracy.

2.4. Mass Profile Reconstruction

The above lensing constraints, together with the physical requirement of $\kappa_{mn} \geq 0$, by themselves are insufficient to constrain the lens uniquely. The fact that the number of lensing constraints is far less than the number of pixels leaves a vast family of mass distributions, all perfectly consistent with the lensing observations. It is now necessary to add more information, based on some criteria for physical plausibility.

As discussed in Paper I, it is particularly interesting to consider mass distributions that minimize

$$\sum_{mn} \left[\left(\sum_{m'n'} \kappa_{m'n'} \right) L_{mn} - \kappa_{mn} \right]^2 + \sigma^4 \sum_{mn} \left(\nabla^2 \kappa_{mn} \right)^2 \quad (2-10)$$

where L_{mn} represents the light profile normalized to unit total luminosity. In Eq. (2-10), the first term tends to minimize the M/L variations while the second term smoothes the mass map on scales of $\leq \sigma$. Such minimization may be considered as regularization with respect to the light distribution and the smoothing scale σ , and is readily implemented via standard numerical algorithms, such as the NAG routine E04NFF. It serves two purposes: (i) as a test whether light is indeed a fair or biased tracer of mass, and (ii) a basis for Monte-Carlo simulations to estimate uncertainties in the mass map. We go into details in the next section, but for now we emphasize strongly that our technique considers the light distribution as a secondary information subservient to the rigid constraints from the observed lensing data.

3. LENSED OBSERVABLES IN ABELL 2218

Abell 2218 is an exceptionally rich lensing cluster, at redshift $z = 0.175$, which hosts 7 multiple image systems and over 100 arclets. In the present paper, we will use all the secure informations that lensing provides in this first application of combined strong and weak lensing. Our analysis of A2218 is based on the archival WFPC2/HST images and we take the redshifts of the resolved images from Ebbels et al. (1998).

Throughout this paper we use $\Omega = 1$; $\Lambda = 0$; $H_0 = 50h$ km/s/Mpc which corresponds to an angular size of $1'' = 3.84$ kpc at the redshift of Abell 2218.

To refer to individual cluster and background galaxies, we will follow the three-digit numbering scheme of Le Borgne et al. (1992); but for objects referred to often we adopt simpler names below.

3.1. Multiply Lensed features

Of the multiply imaged background galaxies, we use the three that have secure spectroscopic redshifts and one with a photometric redshift. Positions and redshifts are listed in Table 1 and plotted in Fig. 2.

ID	z	Image	x	y
384	2.515	a1	14.5	19.1
		a2	17.0	15.4
328	0.702	b1	-14.7	16.1
389	0.702	b2	-17.8	-15.4
289	1.034	c1	-61.7	7.2
		c2	-61.5	0.6
730	1.1	d1	-75.2	-1.4
		d2	-74.6	-6.0
		d3	-73.6	-9.0

Table 1: Positions of various sets of multiple images (x, y in arcsec), as taken from the HST image, used in our reconstruction.

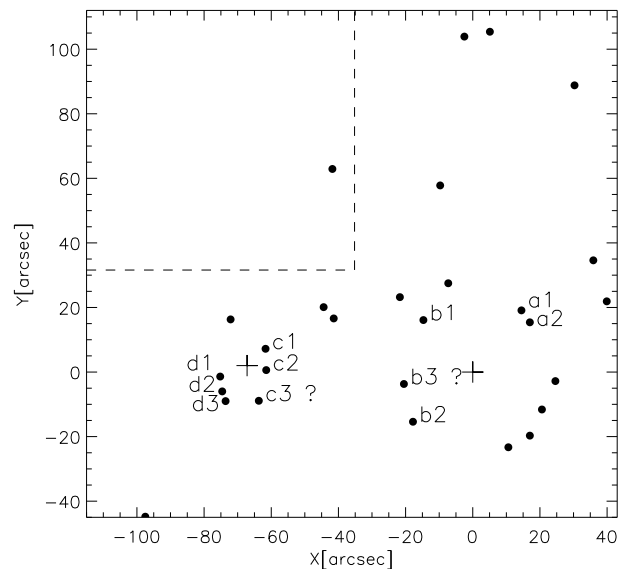


Figure 2. The positions of the multiple images and the arclets in the WFPC2/HST.

- *The ‘a’ system ($z = 2.515$):*

The spectacular arc system #384 clearly shows an internally symmetric pattern of unresolved knots which characterizes the system as a fold arc comprising two merging images (which we will call a1 & a2) with

opposite parities. It is identified to be an image of a background star forming galaxy, with the visible knots representing the H II regions.

- *The ‘b’ system* ($z = 0.702$):

The identification of the multiple images in this system is somewhat complicated. The red arc #359 was initially identified by Pello et al. (1992) to be an image of a background spheroidal galaxy. It was later interpreted by Kneib et al. (1995) using a ground-based image to be two merging images forming a fold arc with #328 as a counter image. However, the improved resolution of HST revealed that such a configuration for the arc #359 cannot be true (KESCS96) since a faint extension connecting it to #337 is now revealed, thus strongly suggesting it as a counter image too. On the other hand, #337 and #389 yield a similar color to #359, thus indicating that #389 is another counter image of #359. Since such a system is complicated and no simple model can explain it, we tried various input configurations. The only plausible solutions can be obtained when #328 and #389 (which we call b1 and b2) are considered as two images from the same source, and #359 (which we call ‘b3?’) is an arclet arising from another source, possibly a different component of the same lensed galaxy.

- *The ‘c’ system* ($z = 1.034$):

The blue arc #289 has a large amount of internal structure in the southern part, which is highly magnified but appears to be slightly distorted and thus characterized to be singly imaged while the tail visible on the north is highly elongated with tiny breaks and definitely multiply imaged. Nevertheless, this complex configuration can be explained by a background source lying near a cusp caustic but with a high portion of it being outside the cusp and observed as the southern end of the arc, while the portion within the caustic is observed as the northern end. We consider the northern part as two merging segments (and call these c1 and c1), and consider the southern part (which we call c3?) as a singly imaged arclet.

- *The ‘d’ system* ($z = 1.1 \pm 0.3$):

This is a faint thin arc, known as #730, with a number of bright knots visible. Three elongated components (which we call d1, d2, and d3) can be easily distinguished along the arc which characterizes it as a cusp arc.

3.2. Secure single distorted arclets:

Ebbels et al. (1998) have spectroscopically measured the redshifts of a number of arclets with different degrees of accuracy in the HST/WFPC2 area. We

use all the arclets for which they have quality-1 redshifts, and arclets with quality-2 redshifts in regions where quality-1 redshifts are not available. Table 2 gives details of the 18 arclets we use. The last two arclets constitute parts of multiple image systems.

ID	z	x	y	θ	ϵ
145	0.628	-2.5	103.9	26.57	2.5
159	0.564	5.1	105.4	80.54	2.0
158	0.723	-41.8	62.9	19.65	2.2
242	0.635	30.3	88.8	117.9	5.0
231	0.563	-9.7	57.8	29.48	4.0
381	0.521	35.9	34.6	157.4	2.5
317	0.474	-7.3	27.5	167.7	1.5
306	0.450	-97.5	-44.8	135.0	1.8
464	0.476	10.6	-23.3	45.0	6.0
467	0.475	17.0	-19.7	48.01	4.0
297	0.450	-21.7	23.2	65.22	5.0
456	0.538	20.6	-11.6	49.76	3.5
238	0.635	-44.4	20.1	49.40	4.0
273	0.800	-41.4	16.6	68.75	2.5
205	0.693	-72.1	16.3	90.00	1.2
431	0.675	39.9	21.9	110.0	6.0
444	1.030	24.6	-2.8	75.96	7.0
359 (b3?)	0.702	-20.5	-3.7	98.75	5.0
289 (c3?)	1.034	-63.7	-8.9	77.20	6.0

Table 2: Observational parameters of the arclets used in our reconstruction. The positions x and y are in arcsec and the position angle θ is in degrees, while ϵ is a lower bound on the elongation. The last two arclets, b3? and c3? are probably parts of the corresponding multiple image systems in Table 1, but we have not used these as multiple-image constraints. We have taken all the arclets as minima of the arrival time, except for b3? which is evidently a saddle.

3.3. Luminosity Distribution

The apparent magnitudes in the R -band of the foreground galaxies are taken from Le Borgne et al. (1992). We considered only those with apparent magnitudes ≤ 20 . and we find that there are 33 of them enclosed within the HST image. The pixellated light distribution L_{mn} is obtained by replacing each of the 33 galaxies by a Gaussian light profile of dispersion $10''$. Fig. 3 shows a contour plot of this smoothed luminosity distribution.

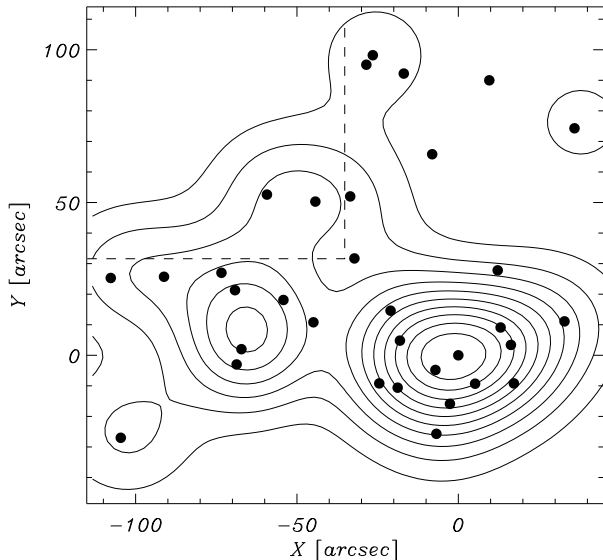


Figure 3. The luminosity distribution of the HST/WFPC2 region of A2218. The positions of the 33 galaxies used are marked with filled circle.

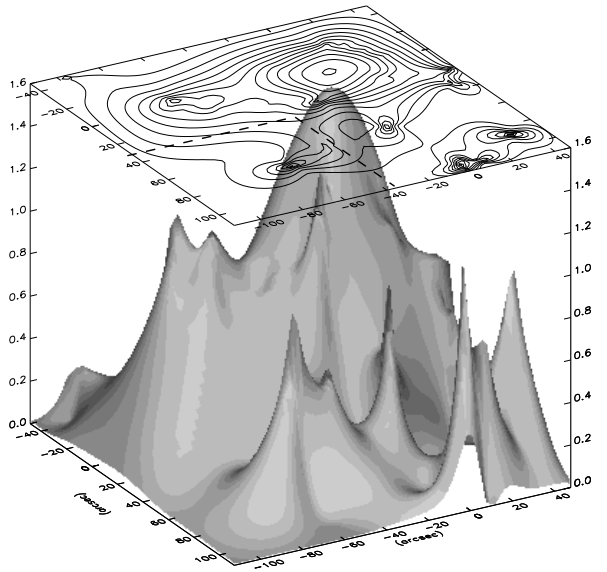


Figure 4. Mass distribution of Abell 2218, reconstructed using strong and weak lensing constraints, and regularizing with respect to the light distribution and a smoothing scale of $6''$. The density is in units of the critical density for sources at infinity, $\Sigma_{\text{crit}} = 3.1 \times 10^{14} h_{50}^{-1} M_{\odot} \text{arcsec}^{-2}$; contours are in steps of 0.1. Later figures in this paper always use the same units, and use the same contour steps unless noted otherwise. The total mass in the field is $2.75 \times 10^{14} h_{50}^{-1} M_{\odot}$.

4. RECONSTRUCTED MASS DISTRIBUTIONS AND UNCERTAINTIES

Our optimal mass map of A2218 is shown in Fig. 4. It uses a pixel size of $2.29''$ and regularizes with respect to the light distribution with smoothing scale $\sigma = 6''$, while strictly obeying all the strong and weak lensing constraints. (We found $\sigma = 6''$ to be the smallest value that eliminated obvious artifacts in the mass map. We use this value throughout this paper except where noted otherwise.) Our mass map is broadly similar to the previous parametric models (K95, KESCS96), which show that the cluster is clearly bimodal with one clump being less massive, and with detailed substructures implied by the lensing data.

It is of interest to examine also other reconstructed mass maps obtained using different criteria. For example, one can reconstruct a mass map by assuming zero light distribution for the cluster (i.e., setting $L_{mn} = 0$ in Eq. 2-10); this is shown in Fig. 5, and is roughly the minimal matter distribution needed to reproduce the data. Or one can reconstruct a mass map with a much higher smoothing parameter; Fig. 6 shows a mass map using $\sigma = 19''$. It is reassuring to see that all the main features are still present in these cases.

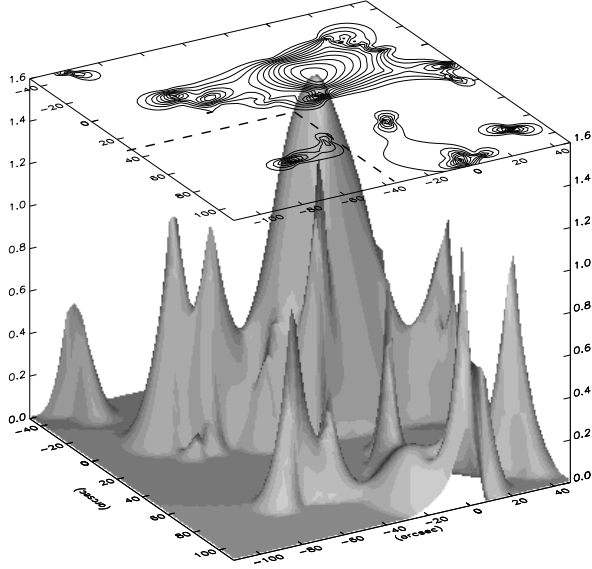


Figure 5. Mass distribution reconstructed for the zero-light case. The total mass in this case is $1.06 \times 10^{14} h_{50}^{-1} M_{\odot}$.

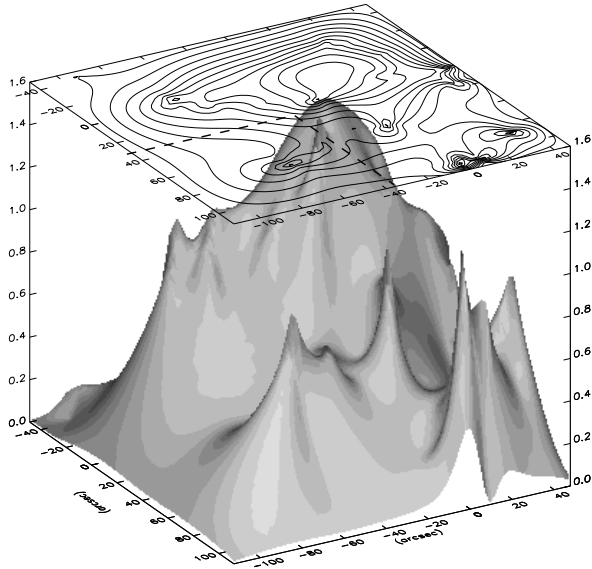


Figure 6. Mass map using much more smoothing: $\sigma = 19''$.

The spikes visible in all our mass maps are due to fact we are using local constraints from sparsely sampled data, i.e., arclets. The peaks of the spikes are very robust between different reconstructions, but the wings are very variable. As a result the total mass shows large variation, though the allowed variation is quite well bounded above and below. Statistical distortion maps going to larger radii would, we expect, constrain the total mass much better and hence reduce this problem. We leave this extension for future work, hopefully with several HST pointings.

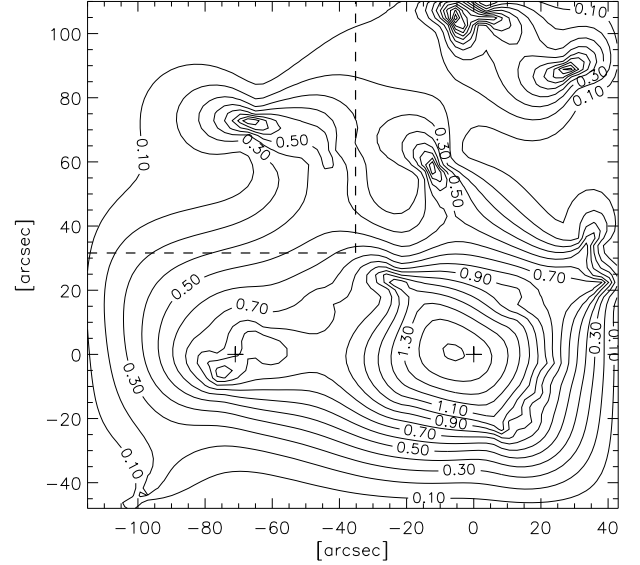


Figure 7. Contour map of the projected mass distribution. This corresponds to Fig. 4 and is plotted here for comparison with Fig. 8.

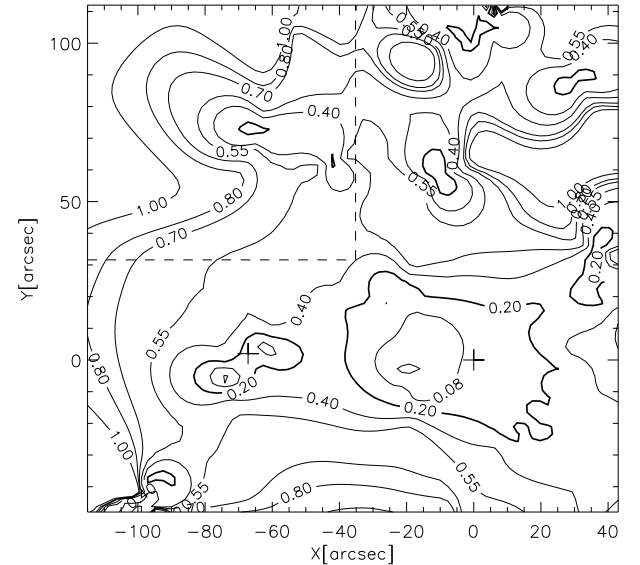


Figure 8. Fractional uncertainty of the mass distribution. The crosses mark the position of the two dominant cD galaxies in A2218.

Our reconstruction technique naturally lends itself towards calculating error estimates on the pixellated mass distribution. We use a Monte-Carlo procedure, randomizing L_{mn} by re-shuffling the positions of the cluster galaxies or by rotating the entire light distribution by various angles, and constructing an ensemble

ble of new mass maps. The fractional dispersion

$$\Delta\kappa_{mn} = \left[\frac{\langle \kappa_{mn}^2 \rangle}{\langle \kappa_{mn} \rangle^2} - 1 \right]^{\frac{1}{2}}. \quad (4-1)$$

over this ensemble is a measure of the pixel-by-pixel fractional uncertainty in the mass map. This is shown in Fig. 8 as a contour plot of the computed $\Delta\kappa_{mn}$. Regions in the lens plane enclosed by $\Delta\kappa_{mn} \leq 0.2$, are very well constrained. Clearly, the best constrained regions have a high number density of images. In Fig. 9 we quantify this by plotting $\Delta\kappa_{mn}$ binned over circles of radius $10''$ versus the the number of images enclosed. As expected, the fractional uncertainty decreases with the number of images.

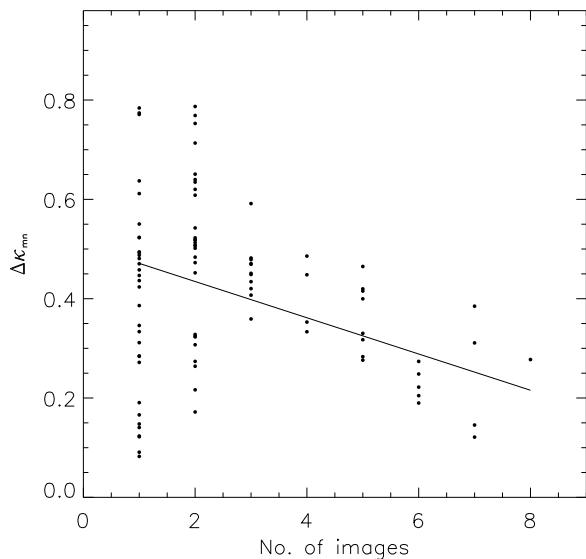


Figure 9. The fractional uncertainty versus the number of images. Each dot represents a circle of radius $10''$ over which $\Delta\kappa_{mn}$ and the number of images have been averaged. The dashed curve is a linear fit.

5. MASS-LIGHT DISCREPANCIES

While our mass reconstruction broadly resembles previous parametric models, we find significant differences that contradict a basic assumption of the parametric modelling method, that of modelling the cluster as a smooth mass distribution plus small clumps associated with bright galaxies. Two of these differences are worth discussing in detail.

First, we find that the highest mass peak is significantly offset from the brightest light peak, the center of the cD galaxy #391. The offset is highly significant given the uncertainties. To test this further, we did a mass reconstruction in a smaller field around this main peak but with a finer pixel size of $1''$. We find (see Fig. 10) that the offset is still persistent and

is about $10''$ towards the second peak of the cluster. It is interesting to note that the direction of the offset between the mass and light peaks detected from our modelling is similar to that found by Markevitch (1997) between the temperature and light peak.

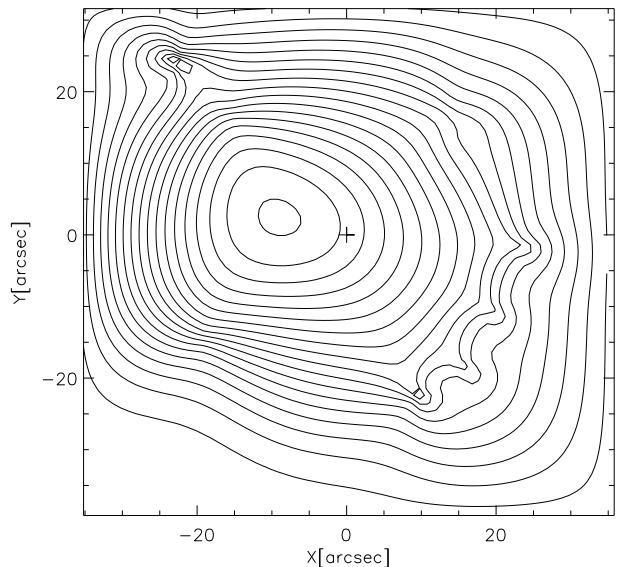


Figure 10. Mass reconstruction of a smaller field, centered on the cD galaxy #391, with $1''$ pixels; a cross marks the cD center.

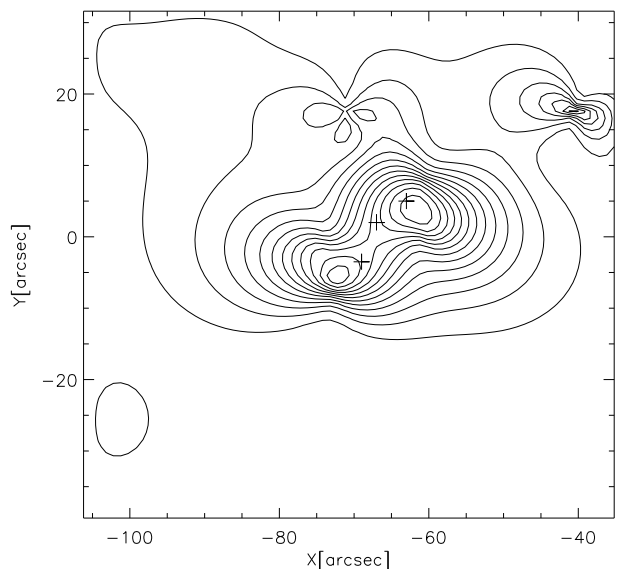


Figure 11. Mass reconstruction of a smaller field centered on the galaxy #244, with $1''$ pixels; crosses mark this galaxy, and two other fainter galaxies.

Second, we find that the secondary mass peak is not centered on the bright galaxy #244. Again, we did a mass reconstruction on a smaller field using $1''$

pixels, this time near #244; this is shown in Fig. 11. The mass distribution in this region, has two peaks in the directions of two galaxies at least 2.5 mag fainter in R than #244, while #244 itself is in a valley between these two peaks. This is also highly significant given the uncertainties, and is seen both in the main reconstruction and in the ‘zoom-in’. If the three mass concentrations are indeed associated with the identified galaxies, the 2.5 mag difference implies that the associated M/L ratios vary by more than a factor of 10.

These new results we reported are robust to pixel size, shape and to the light distribution of the cluster.

6. COMPARISON WITH X-RAY MODELS

The X-ray emission by clusters is usually modelled assuming that the underlying potential of the cluster is spherically symmetric and that the hot gas is in hydrostatic equilibrium. It is important to test these assumptions by comparing with lensing, which does not depend on these assumptions. Miralda-Escudé & Babul (1995) argued that the strong lensing data could not be reconciled with an equilibrium spherical model for the the X-ray emitting gas at the observed temperature—to agree with lensing the gas temperature would have to be much higher, or equivalently, lensing required at least twice as much mass as the gas model. They suggested that the gas might be partly supported by turbulent motion or by magnetic fields, or might be multi-phased. Another possibility is that the cluster is still undergoing a merging phase, and hence the gas would not be expected to trace the gravitational potential.

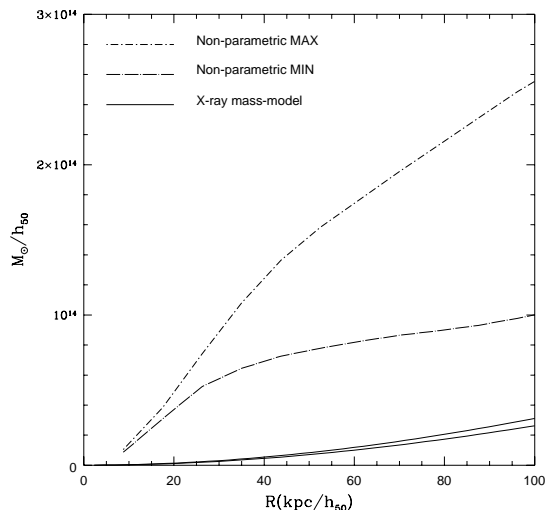


Figure 12. Projected mass within different radii from the main cD galaxy #391, from an X-ray model by Allen et al. 1998 and from lensing. The two lensing reconstructions indicated correspond to Figs 4 (maximum) and 5

(minimum).

In Fig. 12 we plot the enclosed projected mass from a model for the hot gas by Allen (1998) and enclosed mass from our reconstructions. The lowest enclosed mass from lensing we got for the ‘zero-light’ reconstruction shown in Fig. 5; the highest is for our optimal reconstruction (Fig. 4) which tends to minimize M/L variation and thus extrapolates mass into regions with now lensing data; other models correspond to various other regularizations. We see from Fig. 12 that the mass discrepancy is a factor of 2.5 for even the unrealistic-looking model of Fig. 5.

7. ANALYSIS OF INDIVIDUAL MULTIPLE IMAGE SYSTEMS

We have examined the arrival time surfaces, critical curves, and caustics for all the multiple image systems and some of the arclets. Arrival time contours are a good way of verifying a mass distribution reproduces the given image position properties. In this section we discuss two of the multiple image systems in detail, and report predicted counter-images, if any.

7.1. The a1-a2 system

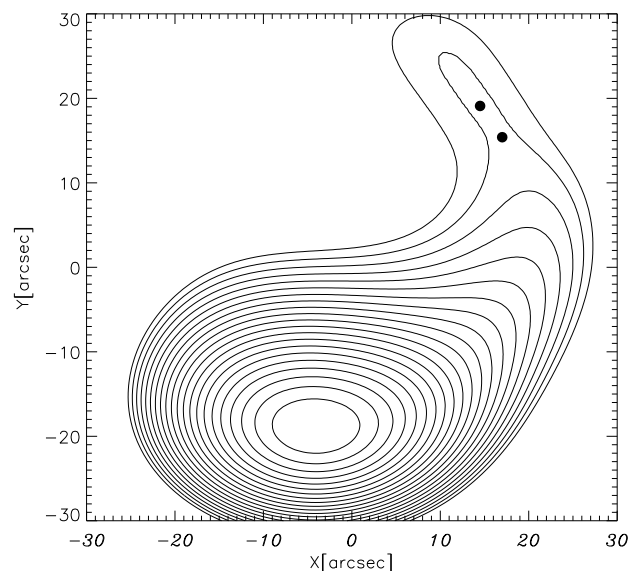


Figure 13. Arrival time surface for the a1-a2 system at $z=2.515$. Filled circles mark the observed positions of a1 and a2. A third image is predicted roughly at $(-5'', -23'')$.

The arrival time surface (see Fig. 13) reproduces the image positions of the two segments a1 and a2 comprising the fold arc. Moreover, the arrival time surface predicts a third image $20''$ below the dominant mass clump, very close to the observed arclet

#468, also predicted by K96 as a counter image for the same arc. The mirror symmetry seen across the arc a1-a2 implies that the critical curve is passing through them. Exploring the critical curves at the redshift ($z = 2.515$) of the system confirms that a1-a2 is indeed a fold arc resulting from a background source lying close to a beak-to-beak caustic. The critical curves and caustics implied by our mass map are shown in Fig. 14.

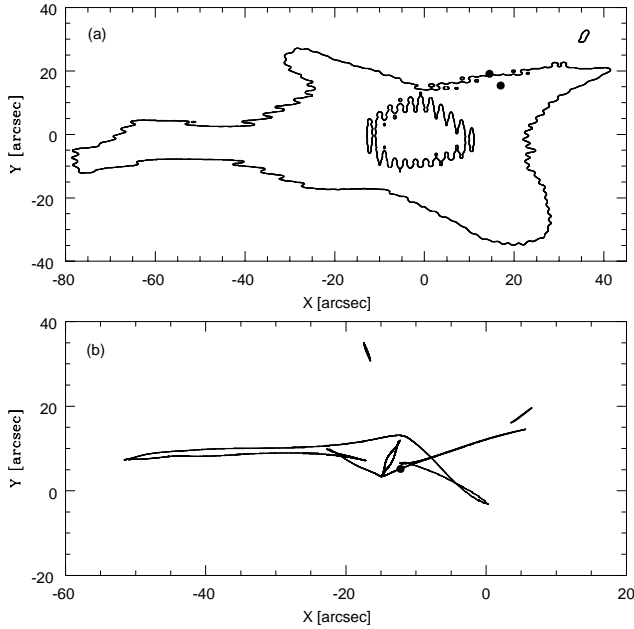


Figure 14. The critical curves and caustics at the redshift of the a1-a2 system ($z = 2.515$). The upper panel shows the critical curves with the two filled circles marking the positions of the two merging images. The lower panel is the corresponding caustics with the filled circle marking the predicted source position.

7.2. The b1-b2 system

The arrival time surface (see Fig. 15) in addition to reproducing the positions of b1 and b2 as required, also predicts an image near the observed position of b3?, but not exactly coinciding with it, which suggests that b3? is an image of a different component of the same lens galaxy. Fig. 16 shows the critical curves caustics at the redshift ($z = 0.702$) of this system. The predicted position of the source is in a region where the caustics are very convoluted and this would result in a complex image configuration. As an auxiliary test, we inspect the arrival time surface for the arclet b3? itself (see Fig. 17). The position of the arclet b3? is of course exactly reproduced and, moreover, four extra images are predicted. The position of two of the predicted images matches fairly with those of the b1, and b2. This result strongly supports the scenario that the images b1, b2 and #337 are counter

images of the arclet b3?.

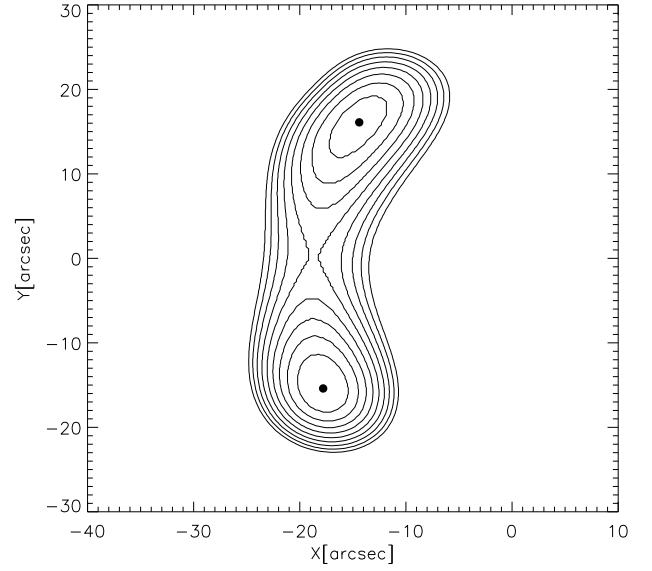


Figure 15. Arrival time surface for the b1-b2 system at $z = 0.702$. Filled circles mark the observed positions of b1 and b2.

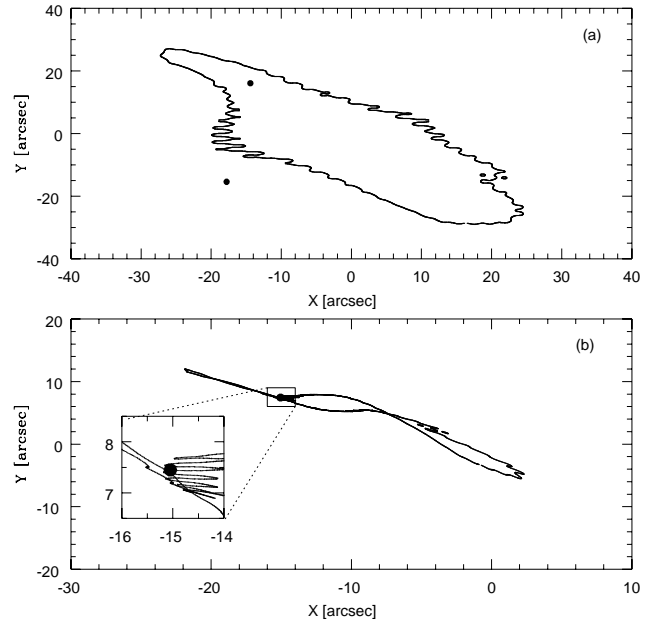


Figure 16. The critical curves and caustics at redshift $z = 0.702$. The critical curve (upper panel) with filled circles marking positions of observed images. Caustics (lower panel) with filled circle marking the predicted position of the source.

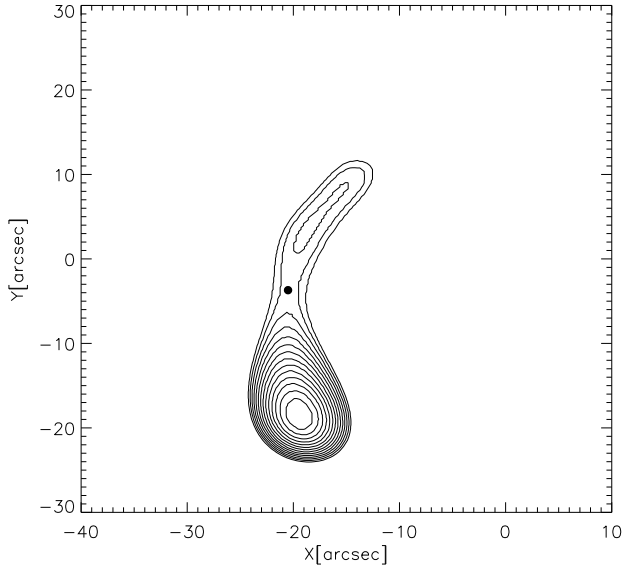


Figure 17. Arrival time surface for b3? at $z=0.702$. The filled circle marks the observed position of b3?.

7.3. Statistical Magnification Map

Since most work on cluster lensing at present is based on statistical distortion of images, it is interesting to examine the statistical magnification map. We calculate the statistical magnification as follows. We first divide the field into square regions of side $10''$ or $20''$. Within each square we compute the magnification matrix at 25 random points, using our optimal mass reconstruction and redshifts randomly chosen from those of the multiply imaged systems; of these we discard any points corresponding to axis ratios > 5 and average the rest. This averaged matrix we call the statistical magnification. Such a procedure roughly mimics the observational procedure of averaging ellipticities while discarding obvious arclets, though of course it is not the same because for real data the absolute magnification is not usually available.

Fig. 18 shows the statistical magnification we obtained by averaging over $10''$ and $20''$ squares. It illustrates a cautionary fact: in the strong lensing region the statistical magnification is dominated by noise. The reason is that a critical curve might be crossed and this can change the shear from ~ 1 to ∞ and back to ~ 1 again over a $10''$ scale. Discarding arclets with high axis ratios does not cure this problem—the left panel in Fig. 18 shows two places with statistical magnification corresponding to axis ratios > 5 even though individual location with such high axis ratios have been excluded; this is because two low-axis-ratio magnification matrices on opposite sides of a critical curve can result in a high-axis-ratio one if averaged.

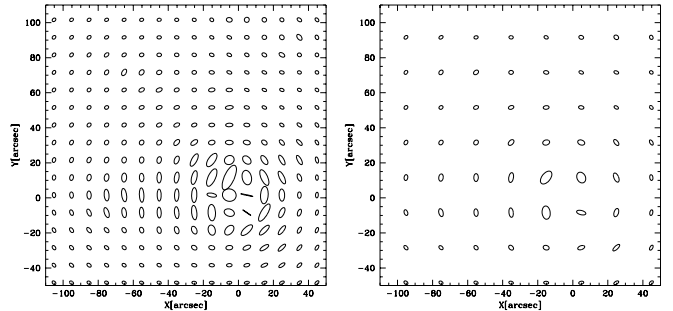


Figure 18. Statistical magnification maps from our optimal mass reconstruction, averaging over $10''$ squares (top), and $20''$ squares (bottom). The size of each ellipse represents the convergence, the shape represents the shear.

We conclude that statistical shear must not be used in the strong lensing region of clusters; instead, constraints from each image should be used separately.

8. CONCLUSIONS

The present paper is, to our knowledge, the first to combine constraints from strong and weak lensing in cluster mass reconstruction. The method we describe recovers a pixellated mass distribution that strictly obeys constraints from lensing observations and uses the light distribution of the cluster as subordinate information that may be overridden by lensing constraints. We explore the projected (dark) matter distribution of Abell 2218 with an unprecedented level of detail. Our mass map shows that the primary mass peak is offset from the the light peak and that projected mass-to-light variations of galaxy-sized components are severely inconsistent with the galaxy M/L scaling deduced from dynamical arguments. In general, these imply that mass does not follow light on a range of length scales in A2218. We also confirm and elaborate a previous result that current X-ray mass models significantly underestimate the mass of a cluster that is able to reproduce the observed lensing. Our results conclude that mass estimates from lensing are *at least* 2.5 times that from X-ray models. This suggests that in at least some clusters intra-cluster hot gas does not trace the gravitational potential.

ACKNOWLEDGEMENTS

The authors would like to thank Steve Allan for providing X-ray mass model of A2218, and Susan Ridgway for reducing the HST archival data. We are also grateful to Ramesh Narayan for an insightful discussion on the mass sheet degeneracy.

HMA acknowledges financial support from the Overseas Research Scheme (ORS), Oxford Overseas Bursary (OOB) and Wolfson College Bursary. LLRW would like to acknowledge PPARC postdoctoral fellowship at IoA, Cambridge.

REFERENCES

- AbdelSalam, H.M., Saha, P. and Williams, L.L.R., 1998, *MNRAS*, **294**, 734
 Allen, S.W., 1998, *MNRAS*, in press (astro-ph/9710217)
 Ebbels, T., Ellis, R., Kneib, J.-P., Le Borgne, J.-F., Pello, R., Smail, I., Sanahuja, B., 1998, *MNRAS*, **295**, 75
 Fort, B. & Mellier, Y., 1994. *A. & A. Rev.*, Volume 5, N0.4, 637
 Kaiser, N. and Squires, G., 1993. *ApJ*, 404, 441
 Kaiser, N., 1995 *ApJ*, 439, L1
 Kneib, J.-P., Mellier, Y., Pello, R., Miralda-Escud/'e, J., Le Borgne, J.-F., Boehringer, H, Picat, J.-P., 1995. *A&A*, 303, 27
 Kneib, J.-P., Ellis, R.S., Smail, I.R., Couch, W., Sharples, R., 1996. *ApJ*, 471, 643
 Le Borgne, J.-f., Pelló, R., Sanahuja, B., 1992. *Astron. Astrophys. Suppl. Ser.*, 95, 87
 Markevitch, M., 1997, *ApJ*, 483, L17
 Miralda-Escudé, J. & Babul, A., 1995. *Apj*, 403, 497
 Seitz, C. and Schneider, P., 1995. *A&A*, 297, 287
 Schneider, P., Seitz, C., 1995. *A&A*, 294, 411
 Squires, G., Kaiser, N., Babul, A., Fahlman, G., Woods, D., Neumann, D. M., Boehringer, H., 1996. *apj*, 461, 572
 Wu, X.-P. and Fang, L.-Z., 1997 *ApJ*, **483**, 62

APPENDIX

INTEGRALS OVER GAUSSIAN PIXELS

Integrating (2-4) yields the coefficient of the mn -th pixel's contribution to the potential:

$$\psi_{mn}(\theta_x, \theta_y) = \frac{a^2}{4} [\ln(u) - \text{Ei}(-u) + \gamma_E], \quad u \equiv \frac{2\theta^2}{a^2}, \quad (\text{A1})$$

where Ei denotes the exponential integral and γ_E is Euler's constant. Thus the first derivatives of the coefficients of the deflection potential, i.e., the components of the deflection angle, are

$$\begin{aligned} \partial_x \psi_{mn}(\theta_x, \theta_y) &= \frac{\theta_x}{u} [1 - \exp(-u)] \\ \partial_y \psi_{mn}(\theta_x, \theta_y) &= \frac{\theta_y}{u} [1 - \exp(-u)]. \end{aligned} \quad (\text{A2})$$

The second derivatives of the potential are

$$\begin{aligned} \partial_{xx} \psi_{mn}(\theta_x, \theta_y) &= \frac{1}{u} \left[1 - \frac{2\theta_x^2}{\theta^2} \right] [1 - \exp(-u)] + \frac{2\theta_x^2}{\theta^2} \exp(-u), \\ \partial_{yy} \psi_{mn}(\theta_x, \theta_y) &= \frac{1}{u} \left[1 - \frac{2\theta_y^2}{\theta^2} \right] [1 - \exp(-u)] + \frac{2\theta_y^2}{\theta^2} \exp(-u), \\ \partial_{xy} \psi_{mn}(\theta_x, \theta_y) &= \frac{2\theta_y \theta_x}{\theta^2} \left[\exp(-u) - \frac{1}{u} [1 - \exp(-u)] \right]. \end{aligned} \quad (\text{A3})$$